Available online at www.sciencedirect.com

ScienceDirect

journal homepage: www.elsevier.com/locate/he

Tunning tin-based perovskite as an electrolyte for semiconductor protonic fuel cells

Nabeela Akbar [a,1], *Sara Paydar* [a,1], *Muhammad Afzal* [b,c], *Muhammad Akbar* [d], *Muhammad Ali Kamran Yousaf Shah* [b], *Wen Ge* [a,**], *Bin Zhu* [a,b,*]

[a] *Engineering Research Center of Nano-Geo Materials of Ministry of Education, Faculty of Materials Science and Chemistry, China University of Geosciences, 388 Lumo Road, Wuhan, 430074, China*

[b] *Jiangsu Provincial Key Laboratory of Solar Energy Science and Technology/ Energy Storage Joint Research Center, School of Energy and Environment, Southeast University, No.2 Si Pai Lou, Nanjing, 210096, China*

[c] *Department of Energy Technology, KTH Royal Institute of Technology, Stockholm, SE, 10044, Sweden*

[d] *Hubei Key Laboratory of Ferro & Piezoelectric Materials and Devices, Faculty of Physics and Electronic Science, Hubei University, Wuhan, 430062, Hubei, China*

HIGHLIGHTS

- Semiconductor $BaSnO_3$ tuned to be a proton conductor.
- Single-phase semiconductor $BaSnO_3$ developed as the functional electrolyte for SPFC.
- $BaSnO_3$ reached a high proton conductivity of 0.23 S cm^{-1} at 550 °C.
- $BaSnO_3$ electrolyte fuel cell has shown high-power output of 843 mW cm^{-2} at 550 °C.

GRAPHICAL ABSTRACT

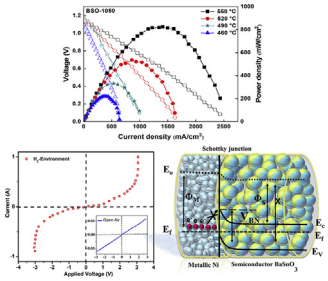

ARTICLE INFO

Article history:
Received 27 September 2021
Received in revised form
18 November 2021
Accepted 19 November 2021
Available online xxx

Keywords:
$BaSnO_3$

ABSTRACT

The use of ceramic semiconductors to serve as an efficient proton conductor is an evolving approach in the novel emerging field of semiconductor protonic fuel cells (SPFCs). One of the most critical challenges in SPFCs is to design a sufficient proton-conductivity of 0.1 S cm^{-1} below <600 °C. Here we report to tune the perovskite $BaSnO_3$ (BSO), a semiconductor single-phase material, to be applied as a proton-conducting electrolyte for SPFC. It was found that the oxygen vacancies play a vital role to promote proton transport while the electronic short-circuiting issue of BSO semiconductor has been justified by the Schottky junction mechanism at the anode/electrolyte interface. We have demonstrated a SPFC device to deliver a maximum power density of 843 mW cm^{-2} with an ionic

* *Corresponding author*. Engineering Research Center of Nano-Geo Materials of Ministry of Education, Faculty of Materials Science and Chemistry, China University of Geosciences, 388 Lumo Road, Wuhan, 430074, China.
** *Corresponding author*.
E-mail addresses: gewen@cug.edu.cn (W. Ge), zhu-bin@seu.edu.cn, zhubin@hubu.edu.cn (B. Zhu).
[1] These authors contributed equally.

https://doi.org/10.1016/j.ijhydene.2021.11.163

Please cite this article as: Akbar N et al., Tunning tin-based perovskite as an electrolyte for semiconductor protonic fuel cells, International Journal of Hydrogen Energy, https://doi.org/10.1016/j.ijhydene.2021.11.163

Perovskite oxide
Semiconductor protonic fuel cell
Oxygen vacancy
Proton transport

conductivity of 0.23 S cm^{-1} for BSO at 550 °C. The oxygen vacancy formation by increasing the annealing temperature helps to understand the proton transport mechanism in BSO and such novel low-temperature SPFC (LT-SPFC).

Introduction

Efficient ion conducting electrolytes and electrodes have always captivated scientists due to their rapid start-up, high power production, and long-term survival of solid oxide fuel cells (SOFC) [1–5]. A principal ionic route used for SOFC electrolytes, like LSGM (Lanthanum Gallate), GDC (Gadolinium-doped ceria) and YSZ (ZrO_2 stabilized 8% Y_2O_3), is diffusion via bulk mostly impacted by the operating temperatures and structural doping [4–9]. To produce thin YSZ electrolyte devices for low-temperature operation diverse advanced thin film technologies have been used, in addition, new materials solve the issues associated to high-temperature operation [10–13]. Recent breakthroughs in perovskite oxides have resulted in the development of innovative techniques allowing perovskites-based low temperature solid oxide fuel cells (LT-SOFCs) with H^+ (proton) conduction. For instance, some ceramic fuel cell performances were well verified at lower temperatures, with significant output of 445 mW cm^{-2} at 500 °C having proton conducting electrolyte BCZYYb ($BaCe_{0.7}Zr_{0.1}Y_{0.1}Yb_{0.1}O_{3-\delta}$) and a ($O^{-2}/H^+/e^-$) triple ion/charge conducting cathode $BaCo_{0.4}Fe_{0.4}Zr_{0.1}Y_{0.1}O_{3-\delta}$ (BCFZY) [14]. Another ground-breaking study on perovskites having H^+ conduction demonstrated that SNO ($SmNiO_3$) with an adequate electronic and ionic conductivity as a SOFC electrolyte can demonstrate a power output up to 225 mW cm^{-2} and an OCV (open-circuit voltage) up to 1.03 V at 500 °C [15]. With electrical conduction reduced by a filling-controlled Mott transition [15], SNO demonstrated the proton conduction between 300 and 500 °C, equivalent to the highest achieved output till date. This intriguing research demonstrated that the H^+ conducting perovskite-oxides are more expected to be operated at lower temperatures that is from 350 °C to 550 °C than conventional electrolytes used for SOFC. Recently, a number of single-phase semiconducting materials have been identified as viable SOFC electrolytes, including LCAO ($Li_{x-}Co_{0.5}Al_{0.5}O_2$) in an arrangement of Ag/LCAO/Ag as a single-layer fuel cell at 525 °C is capable of delivering proton conductivity of approximately 0.1 S cm^{-1} along with the 180 mW cm^{-2} of the power output [16]. Chen et al. claimed that using $SrTiO_3$ as an electrolyte enables a 600 mW cm^{-2} output and that using La–$SrTiO_3$ (LST) as an electrolyte results in a 0.22 S cm^{-1} superoxide ion conductor with a 908 mW cm^{-2} output at 550 °C [17,18]. Additionally, our group has recently revealed superionic surface conduction in CeO_2 and established a mechanism called proton-shuttle at the CeO_2 particles surface, achieving 0.16 S cm^{-1} of proton conductivity and 698 mW cm^{-2} of a high performance at 520 °C [19].

Tin-based perovskites materials have been widely utilized for hydrogen production, Chen et al. demonstrated that $SrSnO_3$ perovskite materials with rod and dumbbell shapes can be successfully employed for splitting of H_2O and an optimal photo-catalytic performance [20]. It has also been reported that BSO with wide-bandgap can sustain electron-mobility (μ) of 320 $cm^2 V^{-1} s^{-1}$ for a single crystal at room temperature and to maintain such mobilities to unusually high electron density. The exceptional mobility at 300 K is expected to rise from a dispersive Sn 5s conduction band in combination with low phonon scattering rates, signifying applications in power electronics and transparent oxides due to its high electronic conductivity [21–23]. Whereas its ionic conduction and fuel cell applications are lacking deeper investigation. Recently materials based on Sn have been studied as operating electrode material for the SOFC application [24]. Thus, these perovskite materials are discovered to be useful in a variety of energy applications and have demonstrated promising outcomes.

The achievement of high-power densities and the identification of charge transport pathways in the mentioned materials keep attracting scientist's attention. Despite of the fact, proton conductors such as $BaZrYO_3$ and $BaCeZrYO_3$ perovskites were invented about 40 years ago, however, their complete understanding of the ion transport mechanism is still unclear [25]. In a seminal publication [26], Goodenough proposed that the primary way to overcome the disadvantages associated with high temperature operation is to shift the focus on novel materials with sufficient ionic conductivity at low temperatures. Taking these facts into account, we used the single-phase tin-based semiconductor perovskite material $BaSnO_3$ (BSO) as an electrolyte to explore the charge transport mechanism at low temperatures of 550 °C. Although our group has employed tin-perovskite-based Co-doped $SrSnO_{3-\delta}$ as an electrolyte membrane for SOFC and obtained 476 mW cm^{-2} power output but the ion types, such as H^+ or O^{2-}, the distinct ionic transport mechanisms in Co-doped $SrSnO_{3-\delta}$ remained unknown [27]. In this work, we have reported that a high proton conductivity could be achieved by tuning a tin-based perovskite BSO, a single-phase semiconductor material, to be applied as an electrolyte membrane. A maximum power density of 843 mW cm^{-2} was achieved by applying the BSO electrolyte for SPFC, which exhibited a high proton conductivity of 0.23 S cm^{-1} for BSO at 550 °C, without any short circuit problem. The proton conduction verification along with the mechanism, and the semiconductor BSO-SPFC device working principle were further investigated.

Experimental

Materials synthesis

$BaSnO_3$ samples were fabricated by a sol-gel method. To prepare 2 g of $BaSnO_3$, firstly an ethylene glycol and $SnCl_4 \cdot 5H_2O$

Please cite this article as: Akbar N et al., Tunning tin-based perovskite as an electrolyte for semiconductor protonic fuel cells, International Journal of Hydrogen Energy, https://doi.org/10.1016/j.ijhydene.2021.11.163

solution was prepared by dissolving 0.1 M of $SnCl_4 \cdot 5H_2O$ (2.30 g) into a 4 M of ethylene glycol (16.31 g) at room temperature. 0.1 M citric acid (12.62 g) was added into the solution, followed by 0.1 M $BaCO_3$ (1.29 g) and agitated at 80 °C to a transparent solution. The resultant solution was heated at 140 °C for 8 h, giving a thick brown gel, which was then kept for auto combustion at 350 °C for 4 h. The resulting powders were grounded and then sintered in air for 4 h at 900 °C, 950 °C, 1000 °C, and 1050 °C respectively. The resultant samples were designated as BSO-900, BSO-950, BSO-1000, and BSO-1050, respectively, and were ready for further characterization.

Fuel cell fabrication

Ni-NCAL ($Ni_{0.8}Co_{0.15}Al_{0.05}LiO_2$)/BSO/NCAL-Ni cells were fabricated by pressing BSO into the center of two Ni-NCAL spherical foams. The NCAL was obtained from China's Tianjin Bamo Science & Technology Joint Stock Co. NCAL paste was prepared by using ethanol, terpineol, and NCAL powder and applied with a brush to nickel foam on one side and kept in oven at 50 °C for 3 h for drying. Which was then used as electrodes with the current collector of Ni attached to it. A BSO based fuel cell was constructed by compacting a homogenous layer of BSO in the middle of two electrodes (Ni-NCAL) for 10 s using a 200 MP uniaxial stress in a configuration of Ni-NCAL/BSO/NCAL-Ni, which was 1 mm thick and have 0.64 cm^2 of active area. The cell was tested after 1 h heat treatment at 550 °C by supplying hydrogen (100 ml min^{-1}) and air (110 ml min^{-1}) as the fuel and the oxidant respectively as shown in Fig. S1.

To verify the H^+ ion conductivity of the BSO-1050, a separate configuration was made with the addition of two $BaZr_{0.1}Ce_{0.7}Y_{0.2}O_{3-\delta}$ (BZCY) layers which act as oxygen-ion-blocking layers that is Ni-NCAL/BZCY/BSO/BZCY/NCAL-Ni.

Material characterization

BSO samples were subjected to X-ray diffraction (XRD) utilizing a Bruker D8—FOCUS X-ray diffractometer (Germany) to identify the crystalline structure. SEM (SU8010, Hitachi Japan) was used to examine the morphology of the samples. The microstructure of the samples, and their elemental/chemical composition, were characterized via an energy dispersive X-ray spectroscope (EDX, SU8010, Hitachi, Japan). XPS (X-ray photoelectron spectroscopy, Escalab 250Xi, Thermo Scientific, Mass, US) was applied to determine the elemental-composition. EIS spectroscopies (electrochemical impedance spectrum) of BSO fuel cells were carried out using an electrochemical workstation (Zennium E, Zahner, Germany). 10 mV (bias voltage) and a frequency range of 1 MHz to 0.01 Hz was applied. Additionally, the *I*—*P* (current-power) and *I*—*V* (current-voltage) characteristics were determined using a ITECH8511tester (ITECH Electrical Co., LTD.).

Results and discussion

Crystalline structure and morphology

The XRD patterns of BSO-1050, BSO-1000, BSO-950, and BSO-900 are presented in Fig. 1. All of the sample's diffraction

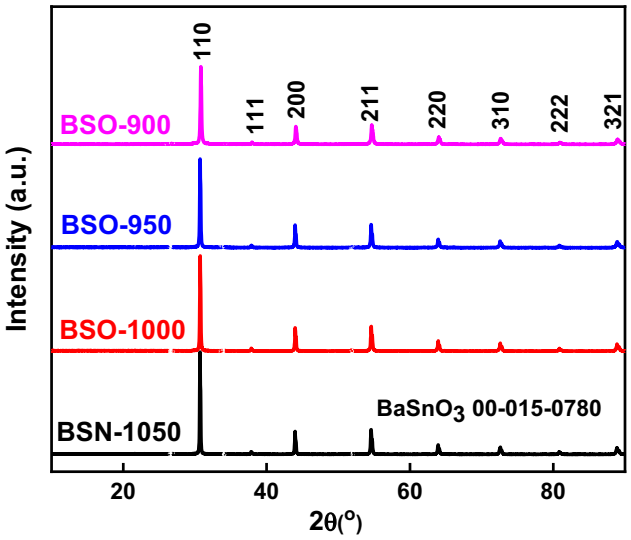

Fig. 1 — XRD patterns of BSO-900, BSO-950, BSO-1000 and BSO-1050.

peaks closely match to the perovskite structures, indicating that no impurity phase was occurred during preparation. The following equation (1) was used to get the crystallite size (*d*).

$$d = K\lambda / (\beta \cos\theta) \quad (1)$$

where K, θ, β and λ are the constant 0.9, peak position, the peak width at half maximum intensity and the wavelength of the radiation, respectively. Using the Scherrer equation the BSO sample's average crystallite sizes were calculated as 63, 70, 76, and 80 nm for BSO-900, BSO-950, BSO-1000, and BSO-1050, respectively. Rietveld refinement analysis of the $BaSnO_3$ XRD data using Maud software is shown in Fig. S2 whereas the Rietveld analysis and the planer indexing are given in Table S1 and S2 respectively. Atomic coordinates and occupancies are given in Table S3. The fitting parameters obtained after the refinement are $\chi^2 = 5.88$, $R_p = 8.9\%$, $R_{wp} = 8.2$.

The SEM images of BSO-900, BSO-950, BSO-1000 and BSO-1050 samples are shown in Fig. 2a-d illustrate the structure and morphology of BSO samples and reveal that the particles are tightly agglomerated, and their rectangular and spherical shape can be seen clearly. In addition, the particle size increases with the increasing annealing temperatures. Whereas microscale SEM image of the BSO-1050 sample in given in Fig. S3. The EDS mapping images of BSO-1050 sample is presented in Fig. 2e-h, which illustrate homogeneous distribution of Ba, Sn, and O elements throughout the specified region.

Fuel cell performance

The *I*—*V* (current-voltage) and *I*—*P* (current-power density) curves of the BSO-1050, BSO-1000, BSO-950, and BSO-900 are presented in Fig. 3a. According to the results the devices achieved a maximum power density of 843 mW cm^{-2} at 550 °C for BSO-1050, which is much higher than the power density of the other samples, which are 687, 610, and 521 mW cm^{-2} for BSO-1000, BSO-950, and BSO-900, respectively. It is clear that the formation of additional oxygen vacancies by increasing the

Please cite this article as: Akbar N et al., Tunning tin-based perovskite as an electrolyte for semiconductor protonic fuel cells, International Journal of Hydrogen Energy, https://doi.org/10.1016/j.ijhydene.2021.11.163

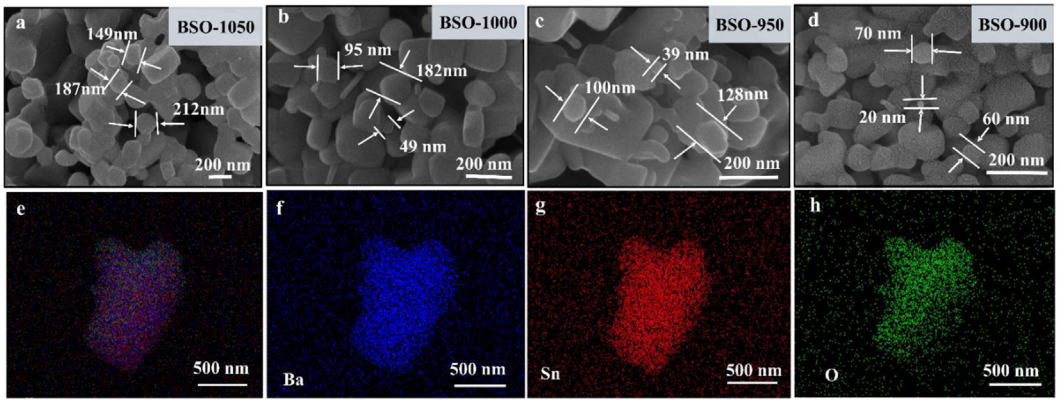

Fig. 2 – SEM images of (a) BSO-1050, (b) BSO-1000, (c) BSO-950 and (d) BSO-900 (e) SEM image of BSO-1050 in higher magnification, and elemental mapping of; (f) Ba, (g) Sn, and (h) O elements.

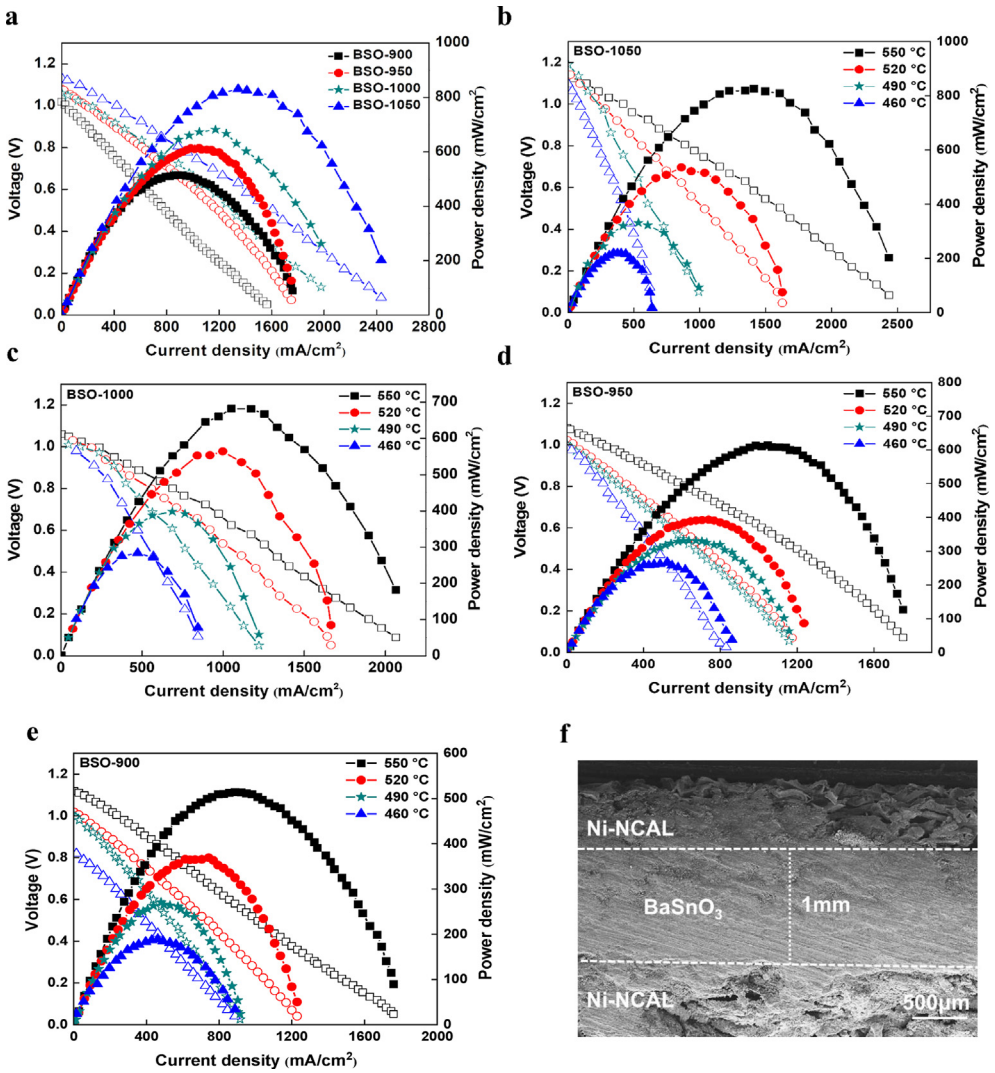

Fig. 3 – (a) Comparing *I*–*V* and *I*–*P* curves of devices based on BSO-1050, BSO-1000, BSO-950 and BSO-900 operated at 550 °C, (b–e) *I*–*V* and *I*–*P* curve of BSO-1050, BSO-1000, BSO-950 and BSO-900 fuel cells at different temperatures, and (f) cross-section SEM image of the fuel cell with (BSO) electrolyte after fuel cell operation at 550 °C.

Please cite this article as: Akbar N et al., Tunning tin-based perovskite as an electrolyte for semiconductor protonic fuel cells, International Journal of Hydrogen Energy, https://doi.org/10.1016/j.ijhydene.2021.11.163

annealing temperature improves the overall BSO-1050 fuel cell operation. This improvement is mainly because of the increased H^+ conductivity of BSO; additionally, H^+ can be electrochemically introduced into the BSO, during fuel cell operation, and H^+ charge carriers reduce the interfacial polarization resistance. As a result, oxygen vacancies increase ion flux, which results in increased power output [19]. The comparison of BSO-1050, BSO-1000, BSO-950, and BSO-900 (Fig. 3a) can clearly depict that the increased annealing temperature has a direct relation with the fuel cell output enhancement. The formation of oxygen vacancies at higher annealing temperature promotes the ion migration resulting in comparatively higher power densities. Fig. 3b–e illustrates further electrochemical characteristics of the BSO-1050, BSO-1000, BSO-950, and BSO-900 as an electrolyte-based cell at various temperatures. These cells demonstrated a power output of more than 500 mW cm^{-2} at 550 °C, thus further supporting the electrolytic function of the BSO. The cross-section SEM image of the fuel cell with BSO electrolyte after fuel cell operation at 550 °C is presented in Fig. 3f. Especially, BSO-1050 fuel cell exhibited a high power density of 843 mW cm^{-2} and the voltage of 1.0 V at 550 °C, and also by decreasing temperature (550–460 °C), the power and OCV outputs decrease marginally, yet 200 mW cm^{-2} and up to 1.0 V is achieved at 460 °C, indicating a good LT-SPFC performance [2,3].

Electrochemical and electrical conductivity analysis

The electrochemical impedance spectrum (EIS) study of BSO based fuel cell at various temperature (460–550 °C) was carried out and the results are shown in Fig. 4. Three contributions which can be realized by AC impedance spectra of a typical solid-ionic conductor material: 1) bulk conduction is reflected by the high frequency arc; 2) the grain boundary by the intermediate frequency arc and 3) the electrode polarization process by low frequency arc [28]. The intercept on the real axis (Z′) is proportional to R_0 at higher frequencies. It is mostly due to the resistance of the BSO layer, which is responsible for ionic and electronic resistances, it increases when annealing temperature decreased. As shown in Fig. 4a, the R_o of BSO-1050, BSO-1000, BSO-950, and BSO-900 samples is 0.12, 0.13, 0.14, and 0.141 Ω cm^2 at 550 °C, respectively. This increase in area resistance values is another strong indication of the ionic conductivity's dependency on the sample annealing temperature. The equivalent circuit shown inside Fig. 4b illustrates the contributions of electrodes (cathode and anode) and electrolyte and Table 1 sums up all the simulated area resistances of BSO-1050. R_o represents the ohmic resistance of BSO-1050 electrolyte. The constant phase elements (CPE) are represented by Q. The in-series elements R_1Q_1 (high frequency arc) and R_2Q_2 (low frequency arc) are owing to the two arcs of the EIS spectra as shown in Fig. 4b. The total resistance (R_t) decreases as the temperature increasing from 460 to 550 °C [29,30]. Additionally, small grain boundary resistances show that BSO-1050 has a high conductivity between 460 and 550 °C, which might be attributed by existence of the high-ionic conduction phase. It can greatly reduce the resistances of the grain boundaries of BSO with the high annealing temperature.

Ionic conductivity

In Fig. 5a the electronic and ionic conductivity dependence of sample BSO-1050 with respect to temperature is illustrated. The total BSO-1050 conductivity (σ_t) at different temperatures was calculated with simulated R_o and R_1 both ionic and electronic resistances are responsible for the total conductivity. Additionally, ionic resistance of BSO samples was determined by the linear slope of the *I–V* curves which can be seen in Fig. 3b, as the ohmic polarization resistance is reflected by the

Table 1 – EIS fitted results of BSO-1050 cell measured at various temperatures under H_2/air atmospheres.

Temperature (°C)	R_o (Ω cm^2)	R_1 (Ω cm^2)	R_2 (Ω cm^2)
550	0.12	0.2	0.32
520	0.14	0.23	0.42
490	0.2	0.22	1.5
460	0.35	0.17	2.6

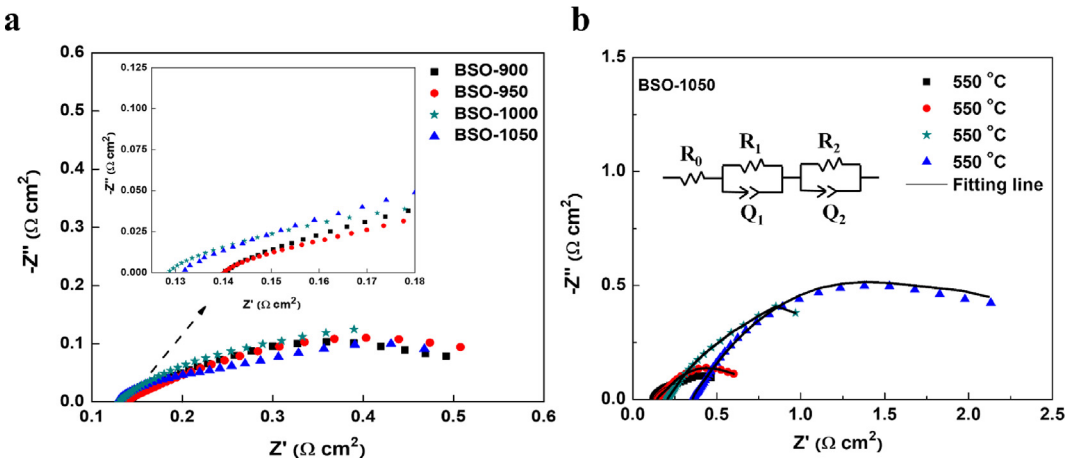

Fig. 4 – (a) Comparing EIS spectra of BSO-1050, BSO-1000, BSO-950 and BSO-900 fuel cells at 550 °C, (b) EIS spectra of the fuel cells based on the samples BSO-1050 at various temperatures.

Please cite this article as: Akbar N et al., Tunning tin-based perovskite as an electrolyte for semiconductor protonic fuel cells, International Journal of Hydrogen Energy, https://doi.org/10.1016/j.ijhydene.2021.11.163

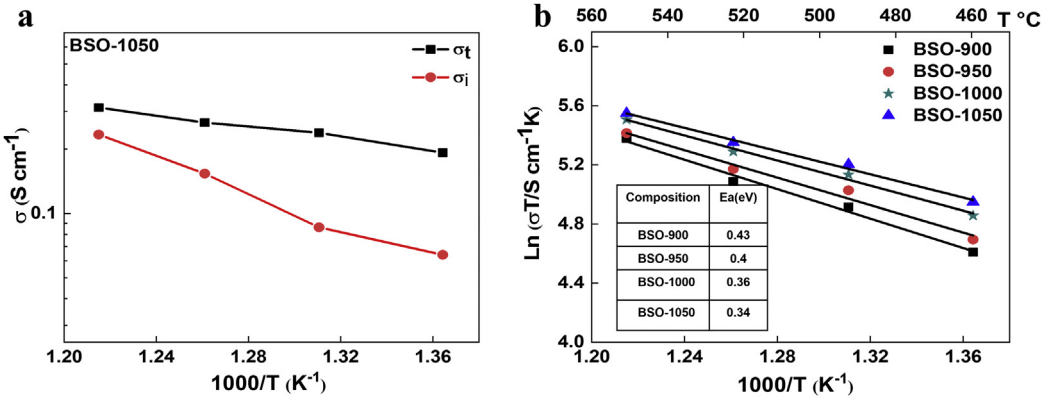

Fig. 5 – (a) Ionic conductivities and electronic conductivities for the BSO-1050 sample as a function of 1000/T, (b) Temperature dependence of the total conductivity of BSO samples.

linear part in the central region, it is primarily determined by the electrolyte's ion transport resistance [31]. At 550 °C, 0.23 S cm^{-1} ionic conductivity of BSO-1050 was obtained, which is significantly higher than that of BSO-1000, BSO-950, and BSO-900, obtained by subtracting the electronic conductivity form the total conductivity (Table 2). This demonstrates that BSO-1050 ion conduction is much higher, which is one order of the magnitude better than that of traditional H^+ conducting materials such as BZY and BZCY under the same conditions [32]. It is claimed that the critical pathway for ion transport in our system relates to increasing oxygen vacancies. Fig. 5b also illustrates the temperature dependence of the BSO-1050 total conductivities. From the linear fit in the temperature range from 550 °C to 460 °C, the activation energy (E_a) of BSO-1050 is calculated to be 0.34 eV which is notably low. At low temperatures, the lower activation energy is due to the lower chemical barrier for the reduction of oxygen which helps the increased electro-catalytic performance [33].

To characterize the type of ion responsible for the fuel cell performance and the role of O^{2-}/H^+ in the BSO-1050 ionic conductivity, the fuel cell device was examined at 550 °C in various atmospheres like H_2–O_2, H_2–N_2 and N_2–O_2 for the electrochemical performance [34]. Fig. 6a illustrates the EIS results for the cell under various atmospheric conditions. Cells exposed to H_2–O_2 have a total resistance of 0.6 Ω cm^2, and for N_2–O_2 and H_2–N_2 atmosphere, total resistances are 2.39 and 0.76 Ω cm^2, respectively. Only H^+ ions can be able to participate in H_2–N_2 atmosphere to the conductivity of the cell, results are implying that protons are responsible for the majority of ionic transport in the BSO-1050 electrolyte. Additionally, we studied and compared the BSO-1050 conductivity in air-air conditions prior to and following the fuel cell operation. It can be seen that at 550 °C a shift from extremely high resistivity to a very low resistivity of 0.5 Ωcm^2 is observed (Fig. 6b). After H_2–O_2 injection, O_2–O_2 was applied and kept for half an hour before testing the EIS and after that N_2–N_2 was applied and held for half an hour prior to testing the EIS. It was observed that the total resistance in O_2–O_2 and N_2–N_2 atmosphere (as shown in Fig. 6c) was lower throughout the test, even after keeping for a long time. This finding also implies that the rapid ion channels and the phase-transformation can be preserved indefinitely, which benefits the cell's stability, whereas the phase-transition is not reversible. In H_2–O_2 atmosphere the oxygen vacancies activation energy is decreased for BSO-1050. Indeed, ion-electron coupling effects the physical characteristics of material substantially, the BSO-1050 super-ionic conduction is caused by the formation of ion defects. The deep ion-electron coupling mechanism needs further investigation in the future work.

To further confirm which type of charge-carrier participate in a BSO-1050 we used the ion separation experiment [35–37]. To prevent the O^{2-} ions migration a BZCY (a well-known protonic material) layer was used in Ni-NCAL/BZCY/BSO-1050/BZCY/NCAL-Ni configuration. This only allows H^+ ion transportation and blocks e^-/O^{2-} to pass through the electrolyte membrane. Thus H^+ ion transport in BSO-1050 can be verified from the *I*–*V* curve displayed in Fig. 6d and the results indicate that our device has proton dominant conduction. It exhibits a Max. power density of 706 mW cm^{-2} and OCV of 1.08 V. Fuel cell performance achieved with BZCY-layers was 84% of that of without BZCY layer. The 16% loss is due to additional interfaces created by introducing the BZCY in the BZCY/BSO-1050/BZCY cell structure, resulting in power losses at interface. This means that actual power output for the device with and without BZCY filters (layers) are comparable.

The above studies on $BaSnO_3$ show the semiconductor possesses some electronic conduction along with the ionic conduction as it can be seen in Fig. 5a. For the conventional electrolyte it is known that internal electronic conduction has negative effect on the SOFCs operation. For that reason,

Table 2 – Comparing ionic conductivities of BSO samples at 550 °C.

Sample	Total conductivity[a] (S cm^{-1})	Electronic conductivity (S cm^{-1})	Ionic conductivity (S cm^{-1})
BSO-900	0.26	0.1	0.16
BSO-950	0.27	0.09	0.18
BSO-1000	0.30	0.09	0.21
BSO-1050	0.31	0.08	0.23

[a] The total conductivity is calculated from EIS results (R_o + R_1) mentioned in Table 2.

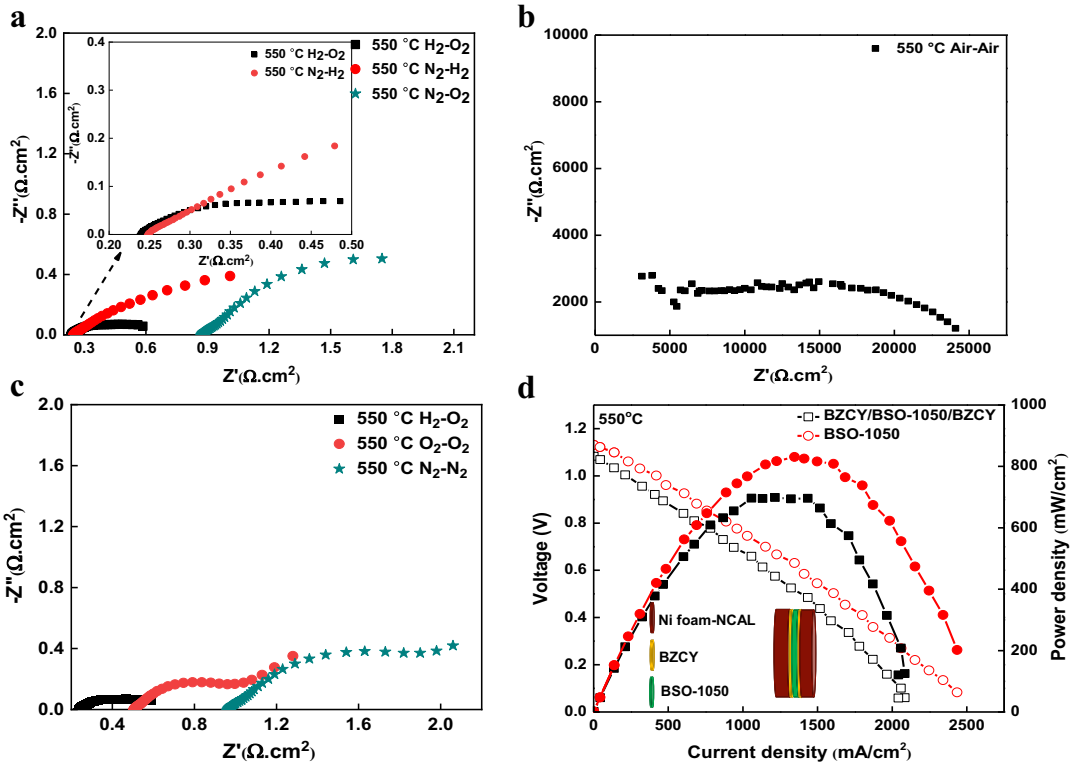

Fig. 6 – (a) EIS spectra of BSO-1050 sample under different atmosphere, (b) EIS spectra of BSO-1050 sample in air (c) EIS spectra of BSO-1050 sample under H_2–O_2, N_2–N_2, O_2–O_2 atmosphere (d) *I*–*V* and *I*–*P* curve of the NCAL-Ni/BZCY/BSO-1050/BZCY/NCAL-Ni.

in conventional fuel cell an electrolyte divider is applied as an electron blocker but in our case the Schottky junction barrier assists to block the electrons to pass the metal and semiconductor interface, which helps to prevent the short-circuit problem. As it is known that the NCAL (anode) is reduced to metallic Ni when placed in hydrogen atmosphere creating a metal-semiconductor contact with the semiconductor $BaSnO_3$ electrolyte, which can build a space-charge region to build a barrier which ceases e^- transport [38]. Mostly, the work functions of semiconductor (Φ_s) and metal (Φ_m) define the nature of metal-semiconductor (M–S) contact. When work functions metal is greater than the work function of semiconductor ($\Phi_m > \Phi_s$) the electrons nearby the metal will migrate from the semiconductor to attain the thermal equilibrium, which creates a barrier height (eV_{BN}) at the interface of M–S to cease the electron transport through the Ni (metal)-$BaSnO_3$ (n-type) semiconductor interface [39]. The *I*–*V* curve of the junction in bias voltage (see Fig. 7a) can confirm the Schottky junction formation. To authenticate this junction formation, the corresponding currents as a function of bias voltage for NCAL-Ni/BSO half-cell were noted under air and H_2 atmosphere at 550 °C on the side of NCAL. At the sides of half-cell, a bias voltage was applied, and the response of current was noted. These operations under air and H_2 conditions models the behavior of the fuel cell before and under H_2 operation. As shown in the Fig. 7a (inset), the current shows a linear behavior in air by varying the bias voltage, which suggests that there is no junction formation in between the NCAL and BSO before operation but as the H_2 was supplied as shown in Fig. 8a, an obvious rectified curve is obtained [40], indicating a Schottky barrier between reduced NCAL anode and BSO electrolyte. This behavior of rectification can be attributed to the formation of the Schottky barrier of anodic Ni and BSO [41]. Fig. 7b presents a schematic diagram of the Ni/BSO Schottky barrier to illustrate the mechanism behind the electron blockage. The Ni/BSO junction barrier height will serve to block the electron to cross the anode/electrolyte interface, and possibly offer an electric field to transport ion [38]. This can partly deduce the reason behind the high-power outputs and OCV despite of having high electronic ion conduction detected in BSO.

Additionally, XPS was implied to determine the electron state of BSO samples. The spectra of BSO-900, BSO-950, BSO-1000, and BSO-1050 samples are shown in Fig. 8a. The spectra of the samples reveal the presence of Ba, Sn, and O elements; the C element seen in the spectra is most likely originated due to the surface-active agent produced between the reaction. O 1s spectra peak values (table S4) at 529 eV and 531 eV in Fig. 8b–e demonstrates the oxygen element's chemical-environment of the oxygen element is notably different in BSO-1050 and other samples, as indicated by deviation of shape and peak position which can be due to the formation of more oxygen vacancies. This O 1s spectra can be subdivided into two distinct components: O_C (chemically absorbed oxygen) and O_L (lattice oxygen) [42].

Please cite this article as: Akbar N et al., Tunning tin-based perovskite as an electrolyte for semiconductor protonic fuel cells, International Journal of Hydrogen Energy, https://doi.org/10.1016/j.ijhydene.2021.11.163

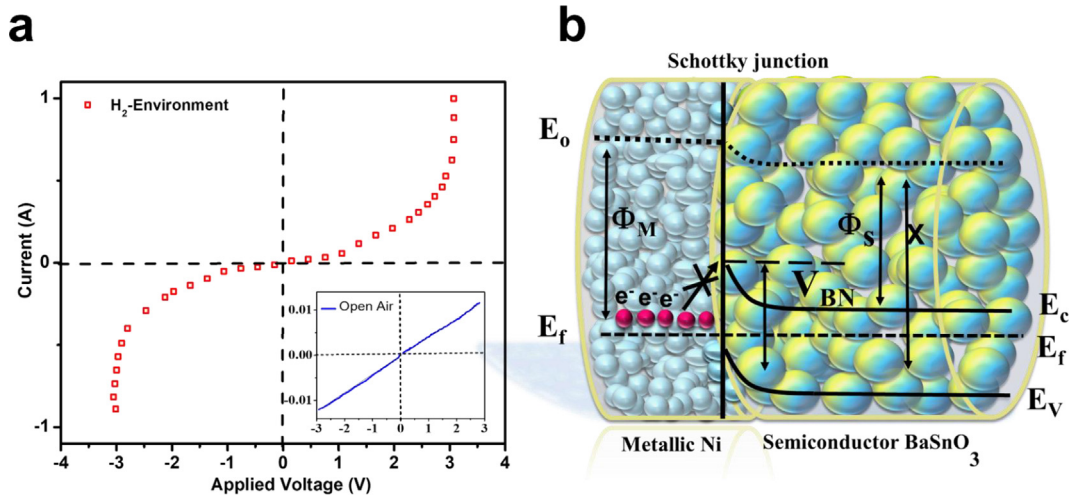

Fig. 7 – The response current as a function of bias voltage for the NCAL-Ni/BSO half cell (a) in H_2 atmosphere and in air (inset). (b) Schematic diagram of the Ni/BSO Schottky junction and energy band structure of BSO fuel cell.

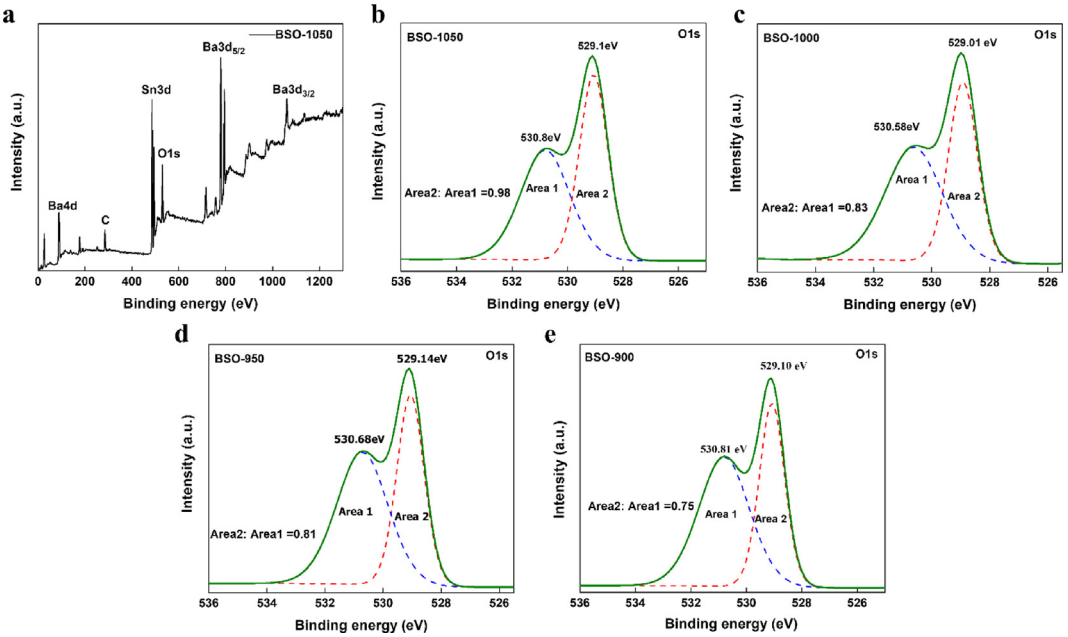

Fig. 8 – (a) XPS spectra of BSO, (b–e) O 1s scan of all 4 samples BSO-1050, BSO-1000, BSO-950 and BSO-900.

Oxygen vacancies can serve as active catalytic sites for H^+ conduction to dissociate water and hydrogen at $BaSnO_3$ surface, resulting in the formation of two hydroxyl form (OH) H^+ defects (Eqs. (2) and (3)).

$$H_2 + 2O_o^x \rightarrow 2OH_o + 2e \quad (2)$$

$$H_2O_{(g)} + V_o^{\cdot\cdot} + O_o^x + \rightarrow 2OH_o \quad (3)$$

This makes BSO an excellent proton carrier, allowing the development of new functionalities based on these features. As shown in Eqs. (2) and (3), oxygen vacancies are vital for proton conduction. Fig. 8b shows that BSO-1050 has the highest oxygen vacancy Area2: Area1 ratio of BSO1050 sample, which is 0.98 to be much higher as compared to 0.83, 0.81, and 0.75 for BSO-1000, BSO-950, and BSO-900, respectively (Fig. 8c–e). The enhancement in the Area2: Area1 ratio with the increase in annealing temperature, reveals that the concentration of oxygen vacancies increases with the annealing temperature [43]. The increase in oxygen vacancies facilitates the proton ion conduction [18]. XPS O 1s spectra demonstrate that all samples have an adequate amount of oxygen vacancy associated with proton transport, the concentration of the oxygen vacancies increases as the annealing temperature increased. The variance of the chemical-environment causes the difference in the position of the lattice oxygen within BSO. It is worth mentioning that the increased oxygen vacancies

Please cite this article as: Akbar N et al., Tunning tin-based perovskite as an electrolyte for semiconductor protonic fuel cells, International Journal of Hydrogen Energy, https://doi.org/10.1016/j.ijhydene.2021.11.163

benefit the material's catalytic activity which eases the proton transport in the fuel cell [44].

Conclusion

This work has demonstrated a new approach to tune semiconducting perovskite BSO to proton conducting electrolyte, which has exhibited a high proton conductivity of 0.23 S cm^{-1} at 550 °C. In addition, we have employed a methodology to improve proton transport via induced oxygen vacancies by controlling annealing temperatures. The annealed BSO at comparatively higher temperature (1050 °C) has displayed highest proton conductivity and device power output than those of other samples BSO-1000, BSO-950 and BSO-900 because the increased oxygen vacancies in BSO-1050 can help to promote proton transport. The BSO-1050 applied as an electrolyte for fuel cell has exhibited an OCV of 1.1 V and power density of 843 mW cm^{-2} at 550 °C. The high OCV near to the theoretical value proves the successful tuning of the semiconductor into a proton conductor. Our work offers a scheme to tune semiconducting perovskite to a proton conductor and a general understanding concerning the enhancement in the proton conduction by aid of the formation of oxygen vacancies which can be controlled by increasing annealing temperature.

Declaration of competing interest

The authors declare that they have no known competing financial interests or personal relationships that could have appeared to influence the work reported in this paper.

Acknowledgements

This work is supported by the National Natural Science Foundation of China (NSFC, grant No. 51772080) and Jiangsu Provincial Innovation and Entrepreneurship Talent program (Project No. JSSCRC2021491).

Appendix A. Supplementary data

Supplementary data to this article can be found online at https://doi.org/10.1016/j.ijhydene.2021.11.163.

REFERENCES

[1] Skinner SJ, Kilner JA. Oxygen ion conductors. Mater Today 2003;6:30–7. https://doi.org/10.1016/S1369-7021(03)00332-8.
[2] Akbar N, Paydar S, Wu Y. Tuning an ionic-electronic mixed conductor $NdBa_{0.5}Sr_{0.5}Co_{1.5}Fe_{0.5}O_{5-d}$ for electrolyte functions of advanced fuel cells. Int J Hydrogen Energy 2021;46:9847–54. https://doi.org/10.1016/j.ijhydene.2020.05.220.
[3] Paydar S, Akbar N, Shi Q, Wu Y. Developing cuprospinel $CuFe_2O_4$-ZnO semiconductor heterostructure as a proton conducting electrolyte for advanced fuel cells. Int J Hydrogen Energy 2021;46:9927–37. https://doi.org/10.1016/j.ijhydene.2020.04.198.
[4] a. Sajid R, Yousaf MAK, Nasir A, Naveed M, Zuhra T, Muhammad Y, Chang PY, Baoyuan W. Tuning semiconductor $LaFe_{0.65}Ti_{0.35}O_{3-\delta}$ to fast ionic transport for advanced ceramics fuel cells. Int J Hydrog Energy 2020;46:9861–73. https://doi.org/10.1016/j.ijhydene.2020.05.155.b. Yamamoto O, Arati Y, Takeda Y, Imanishi N, Mizutani Y, Kawai M, Nakamura Y. Electrical conductivity of stabilized zirconia with ytterbia and scandia. Solid State Ionics 1995;79:137–42. https://doi.org/10.1016/0167-2738(95)00044-7.
[5] a. Francis GK, Stefan TN, Knee Christopher S, Istaq A, Stephen H, Lucienne B, Ivan H, Zhehong G, Frederic B, Clare PG, Sten GE. Crystal structure and proton conductivity of $BaSn_{0.6}Sc_{0.4}O_{3-\delta}$: insights from neutron powder diffraction and solid-state NMR spectroscopy. J Mater Chem A 2016;4:5088. https://doi.org/10.1039/c5ta09744d.
b. Mogensen M, Sammes NM, Tompsett GA. Physical, chemical and electrochemical properties of pure and doped ceria. Solid State Ionics 2000;129:63–94. https://doi.org/10.1016/S0167-2738(99)00318-5.
[6] Lee D, Han JH, Chun Y, Song RH, Shin DR. Preparation and characterization of strontium and magnesium doped lanthanum gallates as the electrolyte for IT-SOFC. J Power Sources 2007;166:35–40. https://doi.org/10.1016/j.matchemphys.2008.06.051.
[7] Varanasi C, Juneja C, Chen C, Kumar B. Electrical conductivity enhancement in heterogeneously doped scandia-stabilized zirconia. J Power Sources 2005;147:128–35. https://doi.org/10.1016/j.jpowsour.2005.01.028.
[8] Zhang J, Paydar S, Akbar N, Yan C. Electrical properties of Ni-doped Sm_2O_3 electrolyte. Int J Hydrogen Energy 2021;46:9758–66. https://doi.org/10.1016/j.ijhydene.2020.08.057.
[9] Paydar S, Peng J, Huang L, Shi Q, Akbar N, Islam QA, Muhammad A, Xing Y, Kim JS, Wu Y. Performance analysis of $LiAl_{0.5}Co_{0.5}O_2$ nanosheets for intermediate-temperature fuel cells. Int J Hydrogen Energy 2021;46:26478–88. https://doi.org/10.1016/j.ijhydene.2021.05.108.
[10] Shao Z, Halle SM. A high-performance cathode for the next generation of solid-oxide fuel cells. Nature 2004;431:170–3. https://doi.org/10.1038/nature02863.
[11] Tao S, Irvine JTS. A redox-stable efficient anode for solid-oxide fuel cells. Nat Mater 2003;2:320–3. https://doi.org/10.1038/nmat871.
[12] Suzuki T, Hasan Z, Funahashi Y, Yamaguchi T, Fujishiro Y, Awano M. Impact of anode microstructure on solid oxide fuel cells. Science 2009;325:852–5. https://doi.org/10.1126/science.1176404.
[13] Evans A, Martynczuk J, Stender D, Schneider CW, Lippert T, Prestat M. Low-temperature micro-solid oxide fuel cells with partially amorphous $La_{0.6}Sr_{0.4}CoO_{3-\delta}$ cathodes. Adv Energy Mater 2015;5:1–9. https://doi.org/10.1002/aenm.201400747.
[14] Duan C, Tong J, Shang M, Nikodemski S, Sanders M, Ricote S, Almansoori A, O'Hayre R. Readily processed protonic ceramic fuel cells with high performance at low temperatures. Science 2015;349:1321–6. https://doi.org/10.1126/science.aab3987.
[15] Zhou Y, Guan X, Zhou H, Ramadoss K, Adam S, Liu H, Lee S, Shi J, Tsuchiya M, Fong DD, Ramanathan S. Strongly correlated perovskite fuel cells. Nature 2016;534:231–4. https://doi.org/10.1038/nature17653.

Please cite this article as: Akbar N et al., Tunning tin-based perovskite as an electrolyte for semiconductor protonic fuel cells, International Journal of Hydrogen Energy, https://doi.org/10.1016/j.ijhydene.2021.11.163

[16] Lan R, Tao S. Novel proton conductors in the layered oxide material $Li_xlAl_{0.5}Co_{0.5}O_2$. Adv Energy Mater 2014;4:1470068. https://doi.org/10.1002/aenm.201301683.
[17] Chen G, Zhu B, Deng H, Luo Y, Sun W, Liu H, Zhang W, Wang X, Qian Y, Hu X, Geng S, Kim JS. Advanced fuel cell based on perovskite La-$SrTiO_3$ semiconductor as the electrolyte with superoxide-ion conduction. ACS Appl Mater Interfaces 2018;10:33179–86. https://doi.org/10.1021/acsami.8b10087.
[18] Chen G, Liu H, He Y, Zhang L, Asghar MI, Geng S, Lund PD. Electrochemical mechanisms of an advanced low-temperature fuel cell with a $SrTiO_3$ electrolyte. J Mater Chem A 2019;7:9638–45. https://doi.org/10.1039/c9ta00499h.
[19] Xing Y, Wu Y, Li L, Shi Q, Shi J, Yun S, Akbar M, Wang B, Kim JS, Zhu B. Proton shuttles in $CeO_2/CeO_{2-\delta}$ core-shell structure. ACS Energy Lett 2019;4:2601–7. https://doi.org/10.1021/acsenergylett.9b01829.
[20] Chen H, Umezawa N. Sensitization of perovskite strontium stannate $SrSnO_3$towards visible-light absorption by doping. Int J Photoenergy 2014;2014:3–6. https://doi.org/10.1155/2014/643532.
[21] Helin W, Abhinav P, Konstantin R, Koustav G, Bharat J, Chris L. Scattering mechanisms and mobility enhancement in epitaxial $BaSnO_3$ thin films probed via electrolyte gating. Apl Mater 2020;8:071113. https://doi.org/10.1063/5.0017227.
[22] Jun L, Zuju M, Rongjian S, Kechen W. Improved thermoelectric power factor and conversion efficiency of perovskite barium stannate. RSC Adv 2017;7:32703. https://doi.org/10.1039/C7RA05193J.
[23] Chang WM, Geunsik L, Kwang SK. La-doped $BaSnO_3$ electron transport layer for perovskite solar cells. J Mater Chem A 2018;6:23071. https://doi.org/10.1039/c8ta08764d.
[24] Wang SF, Hsu YF, Yeh CT, Huang CC, Lu HC. Characteristics of $SrCo_{1-x}Sn_xO_{3-\delta}$ cathode materials for use in solid oxide fuel cells. Solid State Ionics 2012;227:10–6. https://doi.org/10.1016/j.ssi.2012.08.020.
[25] Inna AZ, Liana RT, Gennady KV, Julia GL, Albert RA, Dmitry AM. Heavily Sn-doped barium cerates $BaCe_{0.8-x}Sn_xYb_{0.2}O_{3-\delta}$: correlations between composition and ionic transport. Ceram Int 2021;47:26391–9. https://doi.org/1039/c8ta08764d.
[26] Goodenough JB. Oxide-ion conductors by design. Nature 2000;404:821–3. https://doi.org/10.1038/35009177.
[27] Shah MAKY, Rauf S, Mushtaq N, Yousaf M, Tayyab Z, Akbar N, Ping YC, Wang B. Electrochemical Properties of a Co-doped $SrSnO_{3-\delta}$ based Semiconductor Perovskite used for electrolytes in fuel cells. ACS Appl Energy Mater 2020;3:6323–33. https://doi.org/10.1021/acsaem.0c00521.
[28] Wu Y, Xia C, Zhang W, Yang X, Bao ZY, Li JJ, Zhu B. Natural hematite for next generation solid oxide fuel cells. Adv Funct Mater 2016;26:938–42. https://doi.org/10.1002/adfm.201503756.
[29] Bellino MG, Lamas DG, Walsöe de Reca NE. Preparation and ionic transport properties of YDC–YSZ nanocomposites. J Mater Chem 2008;18:4537–42. https://doi.org/10.1039/B807667G.
[30] Raza R, Liu Q, Nisar J, Wang X, Ma Y, Zhu B. ZnO/NiO nanocomposite electrodes for low-temperature solid oxide fuel cells. Electrochem Commun 2011;13:917–20. https://doi.org/10.1016/j.elecom.2011.05.032.
[31] Lapa CM, Figueiredo FML, de Souza DPF, Song L, Zhu B, Marques FMB. Synthesis and characterization of composite electrolytes based on samaria-doped ceria and Na/Li carbonates. Int J Hydrogen Energy 2010;35:2953–7. https://doi.org/10.1016/j.ijhydene.2009.05.036.
[32] Zhu B, Liu X, Zhou P, Zhu Z, Zhu W, Zhou S. Cost-effective yttrium doped ceria-based composite ceramic materials for intermediate temperature solid oxide fuel cell applications. J Mater Sci Lett 2001;21:591–4. https://doi.org/10.1023/A:1010900829589.
[33] Zuo C, Zha S, Liu M, Hatano M, Uchiyama M. $Ba(Zr_{0.1}Ce_{0.7}Y_{0.2})O_{3-\delta}$ as an electrolyte for low-temperature solid-oxide fuel cells. Adv Mater 2006;18:3318–20. https://doi.org/10.1016/j.jallcom.2008.06.106.
[34] Ding X, Gao Z, Ding D, Zhao X, Hou H, Zhang S, Yuan G. Cation deficiency enabled fast oxygen reduction reaction for a novel SOFC cathode with promoted CO_2 tolerance. Appl Catal B Environ 2019;243:546–55. https://doi.org/10.1016/j.apcatb.2018.10.075.
[35] Zhu B, Huang Y, Fan L, Ma Y, Wang B, Xia C, Afzal M, Zhang B, Dong W, Wang H, Lund PD. Novel fuel cell with nanocomposite functional layer designed by perovskite solar cell principle. Nanomater Energy 2016;19:156–64. https://doi.org/10.1016/j.nanoen.2015.11.015.
[36] Qiao Z, Xia C, Cai Y, Afzal M, Wang H, Qiao J, Zhu B. Electrochemical and electrical properties of doped CeO_2-ZnO composite for low-temperature solid oxide fuel cell applications. J Power Sources 2018;392:33–40. https://doi.org/10.1016/j.jpowsour.2018.04.096.
[37] Xia C, Mi Y, Wang B, Lin B, Chen G, Zhu B. Shaping triple-conducting semiconductor $BaCo_{0.4}Fe_{0.4}Zr_{0.1}Y_{0.1}O_{3-\delta}$ into an electrolyte for low-temperature solid oxide fuel cells. Nat Commun 2019;10:1707. https://doi.org/10.1038/s41467-019-09532-z.
[38] Zhu B, Lund P, Raza R, Ma Y, Fan L, Afzal M, Patakangas J, He Y, Zhao Y, Tan W, Huang Q, Zhang J, Wang H. Schottky junction effect on high performance fuel cells based on nanocomposite materials. Adv Energy Mater 2015;5:1401895. https://doi.org/10.1002/aenm.201401895.
[39] Tschöpe A. Grain size-dependent electrical conductivity of polycrystalline cerium oxide II: space charge model. Solid State Ionics 2001;39:267–80. https://doi.org/10.1016/S0167-2738(01)00677-4.
[40] Saw KG, Tneh SS, Tan GL, Yam FK, Ng SS, Hassan Z. Ohmic-rectifying conversion of Ni contacts on ZnO and the possible determination of ZnO thin film surface polarity. PLoS One 2014;9:86544. https://doi.org/10.1371/journal.pone.0086544.
[41] Young SJ, Ji LW, Chang SJ, Su YK. ZnO metal-semiconductor-metal ultraviolet sensors with various contact electrodes. J Cryst Growth 2006;293:43–7. https://doi.org/10.1016/j.jcrysgro.2006.03.059.
[42] Sharma S, Chhoker S. Efficient light harvesting using simple porphyrin-oxide perovskite system. Sci Rep 2020;10:14121. https://doi.org/10.1038/s41598-020-70554-5.
[43] Ka W, Yong Q, Chang L, Lv L. Effect of annealing temperature on oxygen vacancy concentrations of nanocrystalline CeO_2 film. Appl Surf Sci 2005;351:164–8. https://doi.org/10.1016/j.apsusc.2015.05.122.
[44] Ding X, Gao Z, Ding D, Zhao X, Hou H, Zhang S, Yuan G. Cation deficiency enabled fast oxygen reduction reaction for a novel SOFC cathode with promoted CO_2 tolerance. Appl Catal B Environ 2019;243:546–55. https://doi.org/10.1016/j.apcatb.2018.10.075.

Please cite this article as: Akbar N et al., Tunning tin-based perovskite as an electrolyte for semiconductor protonic fuel cells, International Journal of Hydrogen Energy, https://doi.org/10.1016/j.ijhydene.2021.11.163